OPTICA

X-ray dark-field via spectral propagation-based imaging

JANNIS N. AHLERS,[1,*] **KONSTANTIN M. PAVLOV,**[1,2,3] **MARCUS J. KITCHEN,**[1]
AND KAYE S. MORGAN[1]

[1]School of Physics and Astronomy, Monash University, Clayton VIC 3800, Australia
[2]School of Physical and Chemical Sciences, University of Canterbury, Christchurch 8140, New Zealand
[3]School of Science and Technology, University of New England, Armidale NSW 2351, Australia
*jannis.ahlers@monash.edu

Received 22 September 2023; revised 7 July 2024; accepted 22 July 2024; published 20 August 2024

Dark-field X-ray imaging visualizes scattering from unresolved microstructure. Most dark-field imaging techniques rely on crystals or structured illumination, but recent work has shown that dark-field effects are observable in straightforward propagation-based imaging (PBI). Based on the single-material X-ray Fokker–Planck equation with an *a priori* dark-field energy dependence, we propose an algorithm to extract phase and dark-field effects from dual-energy PBI images. We successfully apply the dark-field retrieval algorithm to simulated and experimental dual-energy data, and show that by accounting for dark-field effects, projected thickness reconstruction is improved compared to the classic Paganin algorithm. With the emergence of spectral detectors, the method could enable single-exposure dark-field imaging of dynamic and living samples.

https://doi.org/10.1364/OPTICA.506742

1. INTRODUCTION

X-ray imaging is a cheap, fast, accessible, high-resolution imaging technique. It is ubiquitous in medical, security, and industrial applications; together, planar and computed-tomography (CT) X-ray scans make up more than 50% of diagnostic medical imaging [1]. However, traditional attenuation-based X-ray imaging has two major drawbacks compared to competing modalities, such as magnetic resonance imaging (MRI) and ultrasound: it comes at a cost of absorbed dose from the ionizing X-rays, and it provides poor contrast in weakly attenuating soft tissues. The advent of high-coherence synchrotron and micro-focus X-ray sources has led to the development of phase-contrast and dark-field X-ray imaging modalities, which supplement attenuation-based contrast [2]. Phase-contrast X-ray imaging measures the refraction of X-rays in the sample, and can achieve significantly improved image quality compared to traditional X-ray imaging, particularly in soft tissue [3]. Dark-field X-ray imaging visualizes the scattered component of the X-ray beam [4,5]. It is associated with small-angle X-ray scattering (SAXS) from unresolved microstructure in the sample, and is a promising candidate for the investigation of such structure. Examples of its use include studying water transport in porous media [6], diagnosis and assessment of pulmonary diseases [7–9] and breast cancer [10], and detection of crystallized urate depositions [11].

A number of techniques have been developed for dark-field imaging. The earliest X-ray dark-field imaging reflected the X-ray wavefield from a rotating crystal to analyze the spread in propagation direction, a technique known as analyzer-based or diffraction-enhanced imaging [12–14]. More recent methods imprint a known reference pattern (structured-illumination/coded aperture) onto the X-ray wavefront, which is then modulated by the presence of the sample, causing changes in amplitude, position, and visibility of the reference pattern (associated respectively with the attenuation, phase-shift, and scattering of the X-rays). If the pixel size is larger than the reference pattern structure, a scanning step is generally used to fully recover the modulation, for example, in Talbot–Lau interferometry [5,15,16] and edge-illumination [17,18]. If the reference pattern is well resolved, modulations can be imaged directly without the need for phase stepping, such as in single-grid imaging [19,20], speckle-based imaging [21,22], and beam-tracking edge-illumination [23].

In these latter direct-imaging techniques, methods of reconstructing phase-shift and dark-field generally fall into "local" or "global" camps, sometimes referred to as "explicit" and "implicit" tracking. Local methods rely on the modulation pattern having "small" (high-frequency) features, usually of order a few pixels; a window around each pixel is applied, and the modulation within that window is explicitly calculated. Examples of this are cross-correlation analysis [20,24] and unified modulated pattern analysis (UMPA) [25] in single-grid and speckle-based imaging. An alternative approach is to model the changes in the wavefront globally, and solve the inverse form of this model for the entire image at once. An example of this is the use of geometric flow [26] and the transport-of-intensity equation (TIE) [27] in speckle-based imaging. The TIE models the coherent flow of optical energy in a propagating paraxial complex-scalar wavefield [28]. An extension of the TIE that includes diffusive flow is the Fokker–Planck equation of X-ray imaging [29,30]. For a z-paraxial plane wave propagating forward after passing through a thin object, the equation can be given in its finite-difference form for the near-field regime as

$$\begin{aligned} I(x, y, z=\Delta) &= I(x, y, z=0) \\ &\quad - \frac{\Delta}{k} \nabla_\perp \cdot [I(x, y, z) \nabla_\perp \phi(x, y, z)]_{z=0} \\ &\quad + \Delta^2 \nabla_\perp^2 [D(x, y) I(x, y, z)]_{z=0}, \end{aligned} \tag{1}$$

where the exit-surface of the sample is at $z=0$, $I(x, y, z)$ is the intensity of the wavefield, Δ is the propagation distance from the exit-surface of the sample to the detector, $k=2\pi/\lambda$ is the wavenumber, λ is the wavelength, $\nabla_\perp \equiv (\partial_x, \partial_y)$ is the transverse gradient operator, $\phi(x, y, z)$ is the phase-shift of the wavefield caused by the object, and $D(x, y)$ is the dimensionless X-ray Fokker–Planck diffusion coefficient, which is related to the angular spread of the dark-field. Excluding the diffusion term from Eq. (1) recovers the finite-difference form of the TIE. The X-ray Fokker–Planck equation can be used to model grating-based imaging [30], and has been used as the basis for novel dark-field retrieval methods in speckle-based imaging [31,32].

A particularly simple X-ray phase-contrast and dark-field imaging technique, which does not require patterning of the wavefront, is propagation-based imaging (PBI). In PBI, an unpatterned spatially coherent wavefront interacts with the sample, and is subsequently propagated through free space. Phase-shifts introduced by the sample cause interference fringes to be developed in the free-space propagating intensity, which are then imaged by a detector [33,34]. PBI does not require specialized optics or a monochromatic source, at the expense of strict spatial coherence requirements [35]. Single-image TIE-based phase-retrieval under a single-material assumption [36] has been extensively applied for phase-contrast PBI, with the single-material assumption not preventing widespread adoption for diverse samples [37]. PBI has recently been extended to dark-field imaging [38–40]. Leatham *et al.* [40] developed a theory of PBI dark-field imaging of a single-material object, based on the Fokker–Planck equation. The method requires imaging a sample at two different propagation distances, relying on the geometric dependence of the scattering cone to separate dark-field effects from attenuation and refraction of the beam. They noted that an alternative approach may be to change the energy of the beam. A multi-energy approach would not require changes in the experimental geometry while imaging, improving ease of implementation and reducing set-up stability requirements. In addition, the recent developments in energy-resolving detectors mean such an approach could capture all the required information within a single exposure.

Dual-energy imaging is a well-established technique dating back to the 1980's [41]. A number of technologies for dual-energy imaging have been developed, such as rapid voltage switching, dual-source CT, and layered detectors [42]. As the attenuation by a specific material is strongly energy-dependent with a theoretically well-grounded dependence, dual-energy imaging establishes a basis for material weighting or decomposition [43]. There are numerous clinical applications of dual-energy imaging, such as measuring bone mineral density, bone removal, and virtual non-contrast imaging [42]. Dual- and multi-energy images have also been utilized in propagation-based phase-contrast imaging, using the TIE as a basis for phase-retrieval [44,45] and material decomposition [46,47]. As dark-field is related to scattering, it has a strong dependence on X-ray energy. This dependence has been exploited in grating-based imaging to recover information about size of the sample microstructure [48–50], to do material decomposition [51], and to improve the signal-to-noise ratio of the recovered dark-field signal [52].

This paper demonstrates a proof-of-concept for spectral propagation-based dark-field imaging (SPB-DF), based on a single-material Fokker–Planck model. Using dual-energy PBI images, the method initially reconstructs the sample's projected thickness. As a second step, the dark-field image is reconstructed by solving the diffusion term in the Fokker–Planck equation for the diffusion coefficient. In addition to using a classic numerical Poisson solver for this step, we introduce a method inspired by structured-illumination dark-field imaging techniques that measures a local change of visibility of the sample, exploiting the texture created by the sample as a "self-reference" pattern. SPB-DF enables optics-free dark-field imaging, without the necessity to move the sample. The potential use of an energy-discriminating detector and polychromatic source with SPB-DF would enable static, single-shot dark-field imaging, with promising applications for imaging dynamic processes.

2. THEORY

Under the Fokker–Planck model, dark-field effects are quantified in the diffusion coefficient D [see Eq. (1)]. Alternatively, a measure of dark-field is the change in visibility V of a reference pattern induced by dark-field blurring. Visibility in a small region of interest around each pixel can be measured as [53,54]

$$V = \frac{I_{\max} - I_{\min}}{I_{\max} + I_{\min}} \approx \frac{\mathrm{StdDev(I)}}{\mathrm{Mean(I)}}. \tag{2}$$

If the reference pattern can locally be modelled as a sinusoidal variation with period p, the visibilities of reference (i.e., no dark-field, V_{ref}) and observed (dark-field present, V_{obs}) images can be related to the Fokker–Planck diffusion coefficient (Eq. 132 in [55], in the case where the dark-field coefficient does not vary significantly over a grid period [30]) via

$$\frac{V_{\mathrm{obs}}}{V_{\mathrm{ref}}} = \exp\left(\frac{-4\pi^2\Delta^2 D}{p^2}\right). \tag{3}$$

Both the size of the window used in the measurement of visibility, and the parameter p used in the conversion to D, depend on the local length scale of features in the reference image. Equation (3) was first derived in the context of speckle and single-grid dark-field imaging, in which there is generally a well-defined length scale associated respectively with the mean speckle size and the grid period. In propagation-based imaging, the beam is not imprinted with a reference pattern. However, if the sample itself creates a relatively quickly varying intensity, this can be treated as a self-reference pattern [40]. For the purposes of this work, we will assume that the length scale of this self-reference pattern is constant throughout the image, and will measure it as twice the full-width at half-maximum of the central peak of a radially averaged 2D autocorrelation—this number is then used as both the window size and period p. This assumption is unlikely to hold for general samples imaged using propagation-based imaging, and in Section 6 we discuss possible methods that could be used in future work to make local estimates of a dominant length scale. In this paper we will reconstruct dark-field images by solving for the Fokker–Planck diffusion coefficient. We will use two approaches to do this, a "global" approach that numerically solves the diffusion part of the Fokker–Planck equation (a Poisson equation) for $D(x, y)$ directly, and a "local" approach that measures visibility in small regions using Eq. (2) and converts it to $D(x, y)$ using Eq. (3).

When two images are taken at relatively low and high energy (cf. large and small propagation distance [40]), dark-field diffusion is much stronger in the lower-energy image. We aim to develop a theory for dark-field reconstruction using dual-energy images, based on the Fokker–Planck equation. To that end, consider a non-crystalline non-magnetic single-material sample being illuminated by a plane wavefield of unit intensity. Assuming a sample with projected thickness $T(x, y)$ and complex refractive index $n = 1 - \delta + i\beta$, with a propagation distance significantly larger than $T(x, y)$, and applying the projection approximation [56], the Fokker–Planck equation [Eq. (1)] becomes

$$I(x, y, z=\Delta) = e^{-\mu T(x,y)} - \frac{\Delta\delta}{\mu}\nabla_\perp^2 e^{-\mu T(x,y)} + \Delta^2\nabla_\perp^2\left[D(x, y)e^{-\mu T(x,y)}\right], \qquad (4)$$

where $\mu = 2k\beta$ is the linear attenuation coefficient. Our aim is to solve Eq. (4) for the projected sample thickness $T(x, y)$ and the Fokker–Planck diffusion coefficient $D(x, y)$, by measuring the propagated intensity $I(x, y, z = \Delta)$ at two different energies. To solve for $T(x, y)$, we begin to linearize Eq. (4) in $T(x, y)$ and $D(x, y)$ by assuming that $D(x, y)$ varies slowly enough that we can neglect higher-order terms, giving $\nabla_\perp^2[D(x, y)e^{-\mu T(x,y)}] \approx D(x, y)\nabla_\perp^2 e^{-\mu T(x,y)}$. We expand the Laplacian [for brevity we drop (x, y) arguments], giving

$$I \approx \left[1 + \left(\frac{\Delta\delta}{\mu} - \Delta^2 D\right)\left(\mu\nabla_\perp^2 T - \mu^2\,\|\nabla_\perp T\|^2\right)\right]e^{-\mu T}, \qquad (5)$$

where $\|\nabla_\perp T\|^2 = \nabla_\perp T \cdot \nabla_\perp T$. Let us assume that the sample is weakly attenuating, with $\mu T \ll 1$. Then for most such samples $\mu^2\|\nabla_\perp T\|^2 \ll |\mu\nabla_\perp^2 T|$, and we can neglect the smaller term. Then we multiply both sides of Eq. (5) by $1 - \mu T$, and neglect higher-order terms in $\mu T\nabla_\perp^2 T$, giving

$$I\frac{1-\mu T}{e^{-\mu T}} \approx (1 - \mu T)(1 + (\Delta\delta - \Delta^2\mu D)\nabla_\perp^2 T) \qquad (6)$$

$$\approx 1 - \mu T + \Delta\delta\nabla_\perp^2 T - \Delta^2\mu D\nabla_\perp^2 T. \qquad (7)$$

In first approximation we assume that $(1 - \mu T)/(e^{-\mu T}) \approx 1$, with the aim of later iteratively correcting this approximation [Eq. (13)]. This gives us a partial-differential equation in two unknown functions $T(x, y)$ and $D(x, y)$, which we can solve using two measurements $I(x, y, z = \Delta)$ at two energies E_1 and E_2. We assume that, for our combination of (monochromatic) energies and sample, the Fokker–Planck diffusion coefficient can be decomposed as $D = D_0\Gamma(\lambda)$, where λ is the wavelength, D_0 is the energy-independent dark-field signal created by the sample, and $\Gamma(\lambda)$ is an unknown function describing the dark-field signal's dependence on energy. Inserting this definition into Eq. (7) and dividing by $\mu\Gamma(\lambda)$, we get

$$\frac{I}{\mu\Gamma(\lambda)} \approx \frac{1}{\mu\Gamma(\lambda)} - \frac{T}{\Gamma(\lambda)} + \frac{\Delta\delta}{\mu\Gamma(\lambda)}\nabla_\perp^2 T - \Delta^2 D_0\nabla_\perp^2 T. \qquad (8)$$

The last term does not depend on energy. Therefore, for two intensity measurements at energies E_1 and E_2 (with corresponding wavelengths λ_1 and λ_2), we can write

$$\begin{aligned} I_1\mu_2\Gamma(\lambda_2) - I_2\mu_1\Gamma(\lambda_1) &= \Delta(\delta_1\mu_2\Gamma(\lambda_2) - \delta_2\mu_1\Gamma(\lambda_1))\nabla_\perp^2 T \\ &\quad + \mu_1\mu_2(\Gamma(\lambda_1) - \Gamma(\lambda_2))T \\ &\quad + (\mu_2\Gamma(\lambda_2) - \mu_1\Gamma(\lambda_1)). \end{aligned} \qquad (9)$$

Denote $\mathfrak{F}[f(x, y)] = \iint_{-\infty}^{\infty} f(x, y)\exp(-2\pi i\vec{r}\cdot\vec{\xi})\mathrm{d}\vec{r}$ as the 2D Fourier transform, with the Fourier-space coordinates $\vec{\xi} = (\xi_x, \xi_y)$ dual to the real-space coordinates $\vec{r} = (x, y)$. We take the Fourier transform of both sides and apply the Fourier derivative theorem, leading to

$$\begin{aligned} \mathfrak{F}[I_1\mu_2\Gamma(\lambda_2) - I_2\mu_1\Gamma(\lambda_1)] &= -4\pi^2|\vec{\xi}|^2\Delta(\delta_1\mu_2\Gamma(\lambda_2) - \delta_2\mu_1\Gamma(\lambda_1))\mathfrak{F}[T] \\ &\quad + \mu_1\mu_2(\Gamma(\lambda_1) - \Gamma(\lambda_2))\mathfrak{F}[T] \\ &\quad + (\mu_2\Gamma(\lambda_2) - \mu_1\Gamma(\lambda_1))\boldsymbol{\delta}(\vec{\xi}), \end{aligned} \qquad (10)$$

where $\boldsymbol{\delta}(\vec{\xi})$ is the 2D Dirac delta function. Finally, we rearrange for $\mathfrak{F}[T]$ and apply the inverse Fourier transform to get

$$T = \mathfrak{F}^{-1}\left[\frac{\mathfrak{F}\left[\mu_2\Gamma(\lambda_2)I_1 - \mu_1\Gamma(\lambda_1)I_2\right]}{f(\lambda_1, \lambda_2, \vec{\xi})}\right] + \frac{\mu_1\Gamma(\lambda_1) - \mu_2\Gamma(\lambda_2)}{\mu_1\mu_2(\Gamma(\lambda_1) - \Gamma(\lambda_2))}, \qquad (11)$$

where

$$f(\lambda_1, \lambda_2, \vec{\xi}) = \mu_1\mu_2(\Gamma(\lambda_1) - \Gamma(\lambda_2)) - 4\pi^2|\vec{\xi}|^2\Delta(\delta_1\mu_2\Gamma(\lambda_2) - \delta_2\mu_1\Gamma(\lambda_1)). \qquad (12)$$

Equation (11) gives an initial estimate $T^{(0)}$ of the sample projected thickness, using two recorded images at two different energies. To improve the estimate, we iteratively correct the left-hand-side in the fully linearized Fokker–Planck equation [Eq. (7)] using

$$I^{(\zeta+1)} = I^{(\zeta)} \cdot \frac{1 - \mu T^{(\zeta)}}{e^{-\mu T^{(\zeta)}}}, \qquad (13)$$

and re-solve for $T^{(\zeta+1)}$, where ζ is the index of iteration. This iterative process can be carried out for a chosen number of iterations, or until a stability criterion is met (see Section 5 and Fig. 2 for further information).

After finding the projected thickness $T(x, y)$, the only unknown left in the single-material Fokker–Planck equation is the diffusion coefficient $D(x, y)$. With only the diffusion term, we are left with a two-dimensional Poisson equation. A variety of methods are available to numerically solve the discrete Poisson equation [55]. Because it is straightforward and computationally inexpensive, we use a de-convolution in Fourier space (see Eq. 13 in [40]) given as

$$D = \frac{e^{\mu T}}{\Delta^2}\nabla_\perp^{-2}\left[I - \underbrace{\left(1-\frac{\delta\Delta}{\mu}\nabla_\perp^2\right)e^{-\mu T}}_{I_{\mathrm{DF-free}}}\right], \tag{14}$$

where the inverse Laplacian $\nabla_\perp^{-2}$ is a pseudo-differential operator of the form

$$\nabla_\perp^{-2} = -\mathfrak{F}^{-1}\frac{1}{4\pi^2|\vec{\xi}|^2+\varepsilon}\mathfrak{F}. \tag{15}$$

The singularity at the origin of the Fourier filter destabilizes the reconstruction at low frequencies, and must be regularized, in this case using a Tikhonov regularization parameter ε. This parameter is fine-tuned for each image to suppress low-frequency artifacts.

We refer to using a numerical solution to the Poisson equation, in our case Eq. (14), as a "global" method of reconstructing dark-field. Alternatively, we could consider a "local" approach based on measuring visibility [Eq. (2)] and converting to $D(x, y)$ using Eq. (3). Equation (3) holds directly for pure-dark-field objects, but does not account for attenuation and phase effects. Our low-energy image I_{E_1} contains a strong dark-field signal, and can act as the "observed" image. A matching "reference" image needs to have identical attenuation and phase effects, but without the dark-field blurring present in I_{E_1}. We can create such an image using our reconstructed projected thickness $T(x, y)$—by simulating a phase-contrast image at the lower energy using a forward model that does *not* include dark-field effects, a "virtual" dark-field-free image is created. An example of such a forward model appears in the inverted Fokker–Planck equation [Eq. (14)]; the term inside the inverse Laplacian denoted $I_{\mathrm{DF-free}}$ is the transport-of-intensity equation propagator, applied to a thin, single-material object [2]. Up to approximation, I and $I_{\text{DF-free}}$ should then be identical anywhere there is no dark-field, but differ proportionally with $\nabla_\perp^2(DI)$, where $D \neq 0$. The visibility maps $V_{\text{obs}}(x, y)$ and $V_{\text{ref}}(x, y)$ can therefore be calculated from I and $I_{\text{DF-free}}$ respectively [using Eq. (2)], and then inserted into Eq. (3) to recover a dark-field image.

3. SIMULATION

An initial validation of the algorithm described in Section 2 was carried out via simulation. A projected thickness map $T_{\text{in}}(x, y)$ was generated [Fig. 1(a)], consisting of the sum of a bulk thickness and a quickly varying texture to simulate a realistic sample. The bulk thickness was created by overlaying three projected superellipsoids, and the quickly varying component of the projected thickness was derived from an X-ray image of a random absorption mask [57,58]. This pattern had a mean period of approximately 10 pixels, measured as twice the full-width at half-maximum of the central peak of a radially averaged 2D autocorrelation. The $T_{\text{in}}(x, y)$ map consisted of 1032 × 1032 pixels with a pixel size of 12 μm.

Complex refractive index values δ and β for poly(methyl methacrylate) (PMMA) at the two chosen energies $E_1 = 25$ keV and $E_2 = 30$ keV were found using `xraylib` [59]. Under the projection approximation, the exit-surface complex scalar wavefield was calculated as

$$\Psi(x, y, z=0) = e^{-kT_{\text{in}}(\beta+i\delta)}. \tag{16}$$

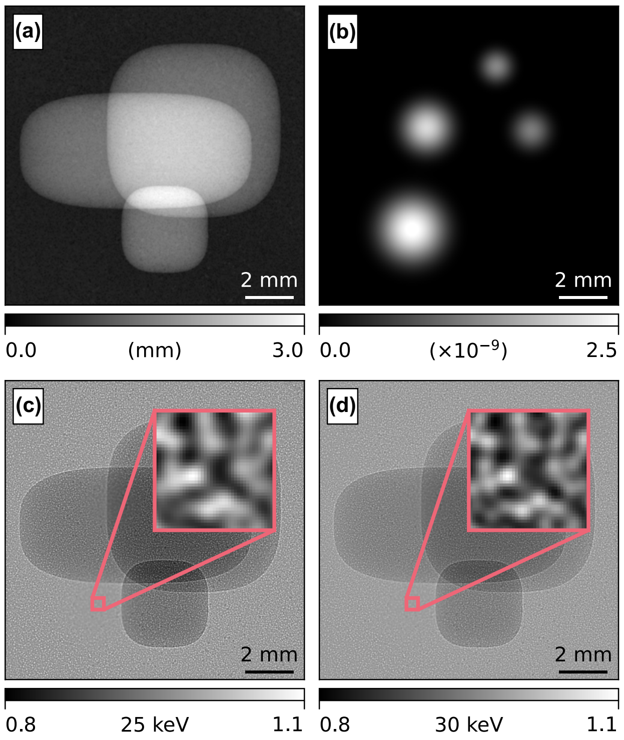

Fig. 1. Simulated data. (a) The projected thickness map $T_{\text{in}}(x, y)$ consists of three superellipsoids, in addition to quickly varying features that cover the entire image. (b) The simulated dark-field signal in the form of the Fokker–Planck diffusion coefficient $D(x, y)$ at 25 keV. The bottom row contains the propagated and dark-field-blurred intensities at (c) 25 keV and (d) 30 keV. To show the difference in local dark-field-associated blurring at the two energies, zoomed insets in (c) and (d) have been included, with their grayscales adjusted to the local minimum and maximum. While the difference is subtle, the reconstruction is able to extract this signal.

The wavefield was then 8× up-scaled using third-order spline interpolation and propagated a distance of $\Delta = 0.5$ m using a Fresnel propagator [2] to create the propagated intensity $I_P(x, y) = |\Psi(x, y, z=\Delta)|^2$. To model an independent dark-field induced blurring, a simulated Fokker–Planck diffusion coefficient $D(x, y)$ at 25 keV was created by overlaying four projected spheres [Fig. 1(b)], and then scaled to 30 keV using an ad-hoc energy dependence of $D \propto \lambda^3$ (see Section 4 for further justification and detail). The diffusion coefficients were converted to blur widths using $\sigma(x, y) = \sqrt{2D(x, y)}\Delta$ [29,30], and finally applied to the propagated intensities $I_P(x, y)$ using a local Gaussian-type diffusion:

$$I(x, y) = \int_{-\infty}^{\infty}\int_{-\infty}^{\infty} I_P(x', y') \times g(x, y; x', y', \sigma(x', y'))\mathrm{d}x'\mathrm{d}y', \tag{17}$$

where $g(x, y; x', y', \sigma)$ is a 2D Gaussian probability density function centered at (x', y'), with standard deviation σ. The resulting simulated images are shown in Figs. 1(c) and 1(d). Where the dark-field signal is present, we see a slight reduction in contrast [see insets in Figs. 1(c) and 1(d)]. This effect is especially pronounced at the lower energy. As we base our reconstruction on the Fokker–Planck model, we deliberately decided not to also use a Fokker–Planck-based forward model for simulation. The

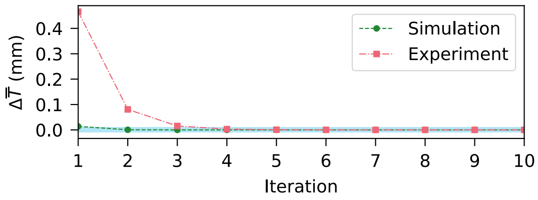

Fig. 2. Difference in mean reconstructed projected thickness between each iteration n of the iterative correction to our algorithm, where $\Delta\bar{T} = \overline{T^{(n)}} - \overline{T^{(n-1)}}$. The shaded area indicates $\pm 10\,\mu\text{m}$. Both simulated (Section 3) and experimental data (Section 5) show rapid convergence.

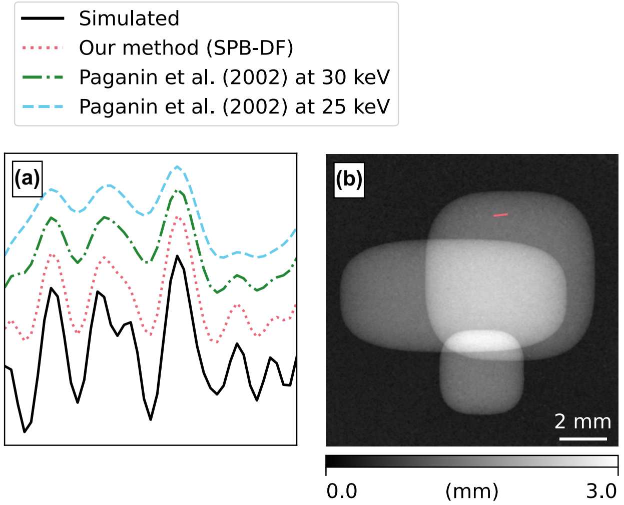

Fig. 3. (a) An intensity line profile comparison between (b) reconstruction of the projected thickness $T(x, y)$ using SPB-DF, and single-material phase retrieval of the 25 keV and 30 keV images based on the transport-of-intensity equation [36]. The solid line shows the simulated projected thickness. By accounting for the strong dark-field diffusion in this part of the sample, SPB-DF improves the fidelity of reconstruction.

approach of Fresnel propagation followed by local diffusion has low computational requirements, is straightforward to implement, and directly simulates the blurring effect seen in experimental propagation-based images. Alternatively, one could simulate dark-field by fully modelling the scattering microstructure. This could be done by ensemble-averaging over the propagated images from many random rapidly varying complex refractive index maps, or by binning the recorded intensity from a high-resolution simulation that directly simulates microstructure.

Using the resulting simulated intensity images, I_{E_1} [Fig. 1(c)] and I_{E_2} [Fig. 1(d)], the projected thickness was reconstructed using Eqs. (11) and (13), with $n = 20$ iterations. A convergence plot for this simulation, as well as for experimental data from Section 5, is shown in Fig. 2; both rapidly converge within approximately five iterations. The resulting projected thickness is shown in Fig. 3(b). In Fig. 3(a) we compare our result to TIE-based projected thickness reconstructions from the simulated images at both energies using an intensity line profile [36]. Although the higher-energy image has the weaker dark-field effects, SPB-DF still achieves better fidelity than either of the TIE-based reconstructions by incorporating dark-field effects in the forward model.

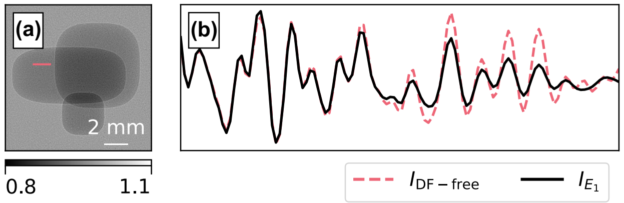

Fig. 4. (a) $I_{\text{DF-free}}$ at 25 keV, created using the reconstructed simulated thickness in Fig. 3(b). (b) An intensity line profile taken along the red line in the first panel, which straddles strong and weak dark-field regions, shows that $I_{\text{DF-free}}$ recovers details that were lost to dark-field induced blurring in I_{E_1} [Fig. 1(c)]. The difference between these profiles is used in the global approach to reconstructing the diffusion coefficient [Eq. (14)], and the change in the local visibility between these two profiles (V_{ref} from $I_{\text{DF-free}}$ and V_{obs} from I_{E_1}) gives a measure of dark-field via Eq. (3) in the local approach.

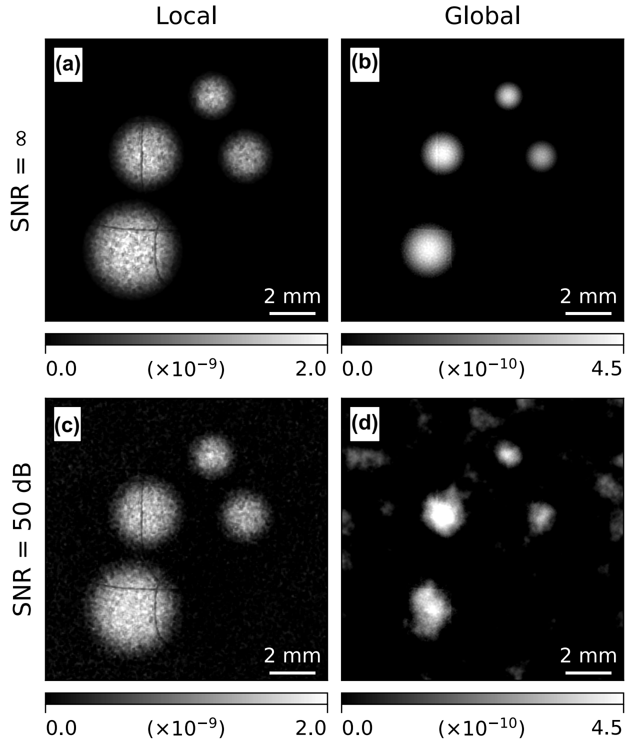

Fig. 5. Reconstructions of the Fokker–Planck diffusion co-efficient (at 25 keV) from simulated data, using a global approach [Eq. (14)] and a local approach [Eq. (3)], with and without added noise. Note that the simulated diffusion coefficient had a range of $0 - 2.5 \times 10^{-9}$ [Fig. 1(b)].

Based on the TIE propagator seen in Eq. (14), the dark-field-free image $I_{\text{DF-free}}$ at the lower energy $E_1 = 25$ keV was created using the reconstructed projected thickness. Figure 4 compares the two key terms in Eq. (14), demonstrating a drop in local image contrast/visibility in the presence of dark-field, as seen in grating/speckle-based methods (e.g., [5,19,24]). Reconstructions of the diffusion coefficient $D(x, y)$ are shown in the top row of Fig. 5, comparing the local [Fig. 5(a)] and global [Fig. 5(b)] approaches described in Section 2. A regularization parameter of $\varepsilon = 2 \times 10^5$ was used in the global reconstruction. For the local reconstruction, visibility was measured in 10×10 pixel sliding windows using Eq. (2), and converted to the diffusion coefficient using Eq. (3) with a period $p = 10$ pixels. The simulation was repeated with zero-mean Gaussian white noise added to the simulated images at a signal-to-noise ratio of $\text{SNR} = 10^5$, with the resulting reconstructions of the diffusion coefficient shown in the bottom row of Fig. 5. Note that all the reconstructions contain some values below zero, which are artifacts from the assumptions made in the theoretical derivation and from the naïve regularization in global reconstruction. For our purposes "negative" diffusion (sharpening) is not considered physically relevant, and so we show all results with the lower gray value set to zero.

Both methods give a reasonable qualitative reconstruction, and the local method is quantitatively close to the original signal. In all reconstructions there are some artifacts remaining from strong phase fringes, where the assumptions of the mathematical treatment in Section 2 break down. As the local method relies on local windowing, the reconstruction looks noisy, even without added noise; by contrast, the global reconstruction is smooth. However, while the local reconstruction is quite robust to added noise, the global reconstruction is sensitive to low-frequency "cloud" artifacts that are typical for this kind of problem [36].

4. DETERMINING DARK-FIELD ENERGY DEPENDENCE

To apply our approach to experimental data, we must decide the Fokker–Planck diffusion coefficient's dependence on energy. To measure this dependence, a dark-field step-wedge phantom was imaged at several energies using single-grid imaging [60] at the Imaging and Medical Beamline (IMBL) of the Australian Synchrotron in Melbourne, Australia. The beamline uses a superconducting multi-pole wiggler insertion device with 1.4 T field strength, and a bent double-Laue crystal monochromator was used to achieve an energy resolution of $\Delta E/E \sim 10^{-3}$ around the chosen beam energy [61]. The sample was placed approximately 135 m downstream of the source, in imaging hutch 3B. An absorption grid, consisting of a stainless steel wire cloth with wire diameter of 61 μm and hole size of 90 μm (Test Sieve; ESSA), was placed upstream of the sample on a movable stage. The sample consisted of a poly(methyl methacrylate) (PMMA) block, which had a central step-wedge shaped void cut out of it and was filled with PMMA microspheres with a diameter of 45–53 μm (DNP-P010; CD Bioparticles). A sample-only image with annotated regions of interest (ROIs) is shown in Fig. 6. A 2 m sample to detector distance was set. The detector used was IMBL's "Ruby", consisting of a 25 μm Gd_2O_2S:Tb scintillator coupled to a PCO.edge sCMOS sensor (16-bit, 2560 × 2160 pixels) via a lens system, giving an effective pixel size of 5.6 μm. The sample was imaged at energies of 25, 27.5, 30, 32.5, 35, 37.5, 40, 42.5, and 45 keV.

At each beam energy we recorded 30 grid-only, sample and grid, flat-field, and dark-current images. Images were averaged, and flat-field and dark-current corrected. We found that the grid and sample both independently moved up to 5 to 10 pixels between energies. This could have been due to backlash error from repeated movement of the sample and grid stages into and out of the beam, as well as from the beam angle changing slightly when changing energy. Images were registered to the grid pattern using enhanced correlation coefficient (EEC) maximization [62]. A small remaining movement of the sample between energies remained, but did not significantly affect the results as the final step in processing was an averaging over large regions of interest.

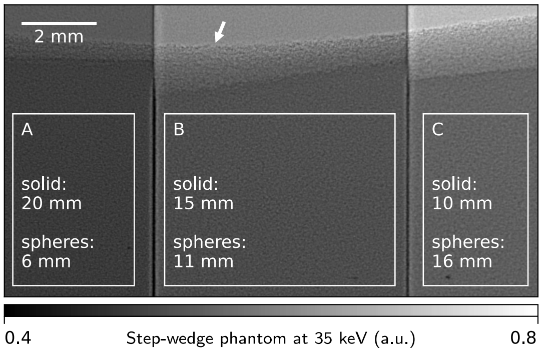

Fig. 6. Regions of interest (A)–(C) shown on 35 keV PBI image of a PMMA step-wedge phantom. The regions consist of increasing depths of 45–53 μm diameter PMMA microspheres (and decreasing depths of solid PMMA). All thicknesses have an uncertainty of ±1 mm. The arrow marks the uneven top surface of the microspheres.

A single-grid reconstruction method was used to measure the dark-field signal in different ROIs of the sample at different energies [60]. The method applies a local cross-correlation at each pixel between a small kernel in the sample-and-grid image, and a larger search region in the grid-only image. A sinusoid model of the grid is used to fit the data to the cross-correlation, giving the attenuation and relative change in visibility δV (denoted "DF" in Eq. 7 of [60]) induced by the sample at each pixel. Finally, a median filter with size of the grid pitch is applied. The resulting reduction in V was converted to a Fokker–Planck diffusion coefficient using Eq. (3). Note that this is equivalent to an initial conversion to a scattering angle θ according to Eq. 11 in [60], which is directly related to the diffusion coefficient [55]. The mean Fokker–Planck diffusion coefficient in each ROI measured this way is plotted against wavelength in Fig. 7. To model the energy dependence of the diffusion coefficient a power law of the form $D(\lambda) = a\lambda^b$ was chosen, which has been demonstrated in theory [51,55], simulation [63], and experiment [50,51] to be a good fit for dark-field diffusion energy dependence in a variety of models (such as hard-spheres [51,55] and random walk through random media [55]) and samples (both packed spheres and more complex microstructure [51,63]). The model, with the four free parameters a_i and b (where $i \in \{1, 2, 3\}$ indexes the three ROIs), was fit to all measurements simultaneously using the Levenberg–Marquardt algorithm. The factors a_i are expected to contain information about the projected thickness of microspheres in each region (alternatively, the number of scattering interfaces), and are assumed to be independent of energy. The resulting energy dependence was $b = 3.72 \pm 0.03$. This result is broadly consistent with previous measurements of dark-field energy dependence in grating interferometry [50,51]. An in-depth comparison would need to consider the difference in origin and measurement of dark-field signal, in

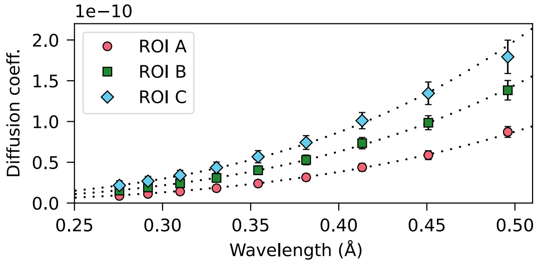

Fig. 7. Mean Fokker–Planck diffusion coefficient D in each region of interest (ROI) (A)–(C) of the step-wedge phantom (illustrated in Fig. 6) at each energy, measured using single-grid imaging. The error bars show the standard deviation in a region. The results are simultaneously fit to a power law model of the form $D_i(\lambda) = a_i\lambda^b$, where λ is the wavelength, i denotes each region, and a_i and b are four free parameters. The resulting energy dependence is $b = 3.72 \pm 0.03$.

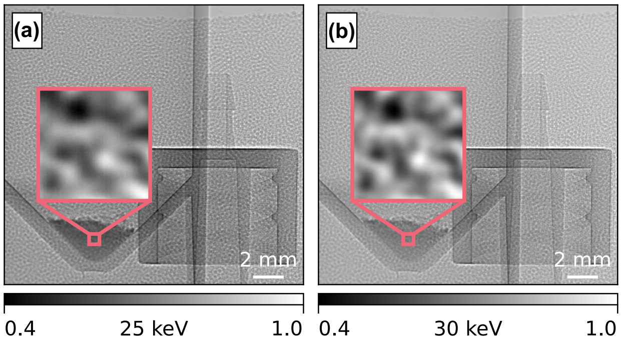

Fig. 8. Experimental images of an approximately single-material sample at (a) 25 keV and (b) 30 keV. Most of the sample is composed of solid plastic, except for a powder of 1 μm diameter polystyrene microspheres in the test tube at the bottom left of the images. There is a subtle but perceptible difference in the blurriness of the sample's texture in the region of the powder at the two energies.

both the propagation-based and interferometric context, but is beyond the scope of his article. This is an active area of research in the literature (see, e.g., [55]), and we emphasize that this dependence is likely to depend on details of the sample and experimental set-up. An updated understanding of dark-field energy dependence could be incorporated into $\Gamma(\lambda)$ without alteration to the body of the SPB-DF algorithm.

5. EXPERIMENTAL DEMONSTRATION

Experimental images were taken at IMBL, with the wiggler field strength adjusted to 3 T. The sample consisted of a plastic test tube containing polystyrene microspheres with a diameter of 1 μm (P/N 100211-10; Corpuscular), placed next to a solid plastic male Luer lock adaptor. Directly in front of these was placed a custom made PMMA container, which was filled with 250–300 μm diameter PMMA microspheres (Cospheric) to provide a consistent dominant local length scale. The container had walls of 2 mm thickness, with a 1 mm gap between them.

As in Section 4, the IMBL's "Ruby" detector was used, with an effective pixel size measured at 9.7 μm. The sample was placed at a propagation distance of 3.5 m, and imaged at 25 keV and 30 keV. Images were flat-field and dark-current corrected, and registered using EEC maximization [62]. The resulting images are shown in Fig. 8. As in the simulation, a slight blurring of the quickly varying structure can be seen through the 1 μm microspheres, which varies with energy. In a region containing only the large microspheres, a measurement of local length scale gave $p = 15.7$ pixels.

The results of reconstructions of the experimental sample can be seen in Fig. 9. The dark-field energy dependence of $D \propto \lambda^{3.72}$ found in Section 4 was used in the reconstruction of the projected thickness [Fig. 9(a)]. As in the simulation, the thickness was also reconstructed using the TIE-based Paganin algorithm at each of the two energies [36]. A line profile of T through the region of the sample with the strongest dark-field signal is shown in Fig. 9(b), comparing the thickness reconstructions. While, unlike in the simulation [Fig. 3(a)], the true sample thickness is unknown, the trend of an improved visibility of features in the projected thickness reconstruction is the same as in the simulation. For the global dark-field reconstruction [Fig. 9(d)], a regularization parameter of $\varepsilon = 2.88 \times 10^7$ was found to be optimal. The global reconstruction clearly differentiates the strongly scattering 1 μm microspheres from the rest of the sample, with almost no obvious artifacts. In contrast, the local reconstruction [Fig. 9(c)] retains some artifacts from the strong phase edges on the Luer lock and test tube.

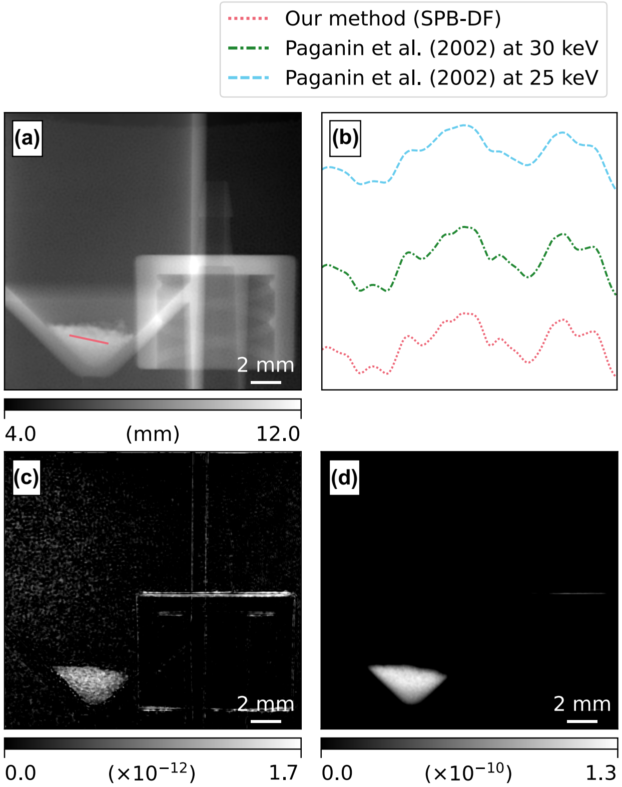

Fig. 9. Reconstructions from the experimental data. (a) While all objects can be seen in the projected thickness reconstruction, only the 1 μm diameter polystyrene microspheres are prominent in (c) local and (d) global dark-field reconstructions. While the local dark-field reconstruction contains some artifacts from the strong phase edges of the Luer lock, the global reconstruction is almost free of artifacts. (b) The projected thickness line profile along the red line shown in (a) compared to projected thickness reconstructions using the TIE-based Paganin algorithm [36] at each energy.

6. DISCUSSION

Our method of dark-field imaging involves two steps: (1) the projected thickness of the sample is reconstructed, taking into account dark-field effects; and (2) based on the projected thickness, the Fokker–Planck diffusion coefficient is reconstructed. This first step provides the opportunity to improve the resolution and feasibility of the microscopy of samples with porous or granular regions [64]. For the second step, we have considered two approaches. A global approach is to numerically solve the diffusion part of the Fokker–Plank equation, a Poisson equation. While we have used a straightforward spectral solution with a manually optimized Tihkonov regularization, more advanced regularization schemes or numerical methods of solving the Poisson equation that may be more appropriate for this kind of diffusive dark-field reconstruction could be explored in future work. In addition to this global approach, we have suggested an alternative approach that is inspired by structured-illumination techniques, based on comparing the visibility of local features. In this case, we compare the visibility of a small region around each pixel in one image that contains strong dark-field effects (the raw, lower-energy image) and another that contains none ($I_{\mathrm{DF-free}}$, created using the reconstructed projected thickness).

We must emphasize that a reconstruction based on local visibility relies on local structure being present in the images, and on this local structure varying over a few pixels. Quantitative local reconstruction depends on knowing the period of local intensity variation. In the simulation and experiment we deliberately included a rapidly varying and consistent texture in the sample. However, a generic sample will not in general create a well-defined intensity variation of consistent size/period. This could be addressed by first estimating a local period (e.g., using a 2D wavelet transform), and then adjusting the window size and period at each pixel accordingly. In Section 1 of Supplement 1 we repeat both the simulation and experiment carried out in this paper, but do not deliberately include quickly varying features in the samples. While a global inversion of the Fokker–Planck equation is able to reconstruct dark-field even when there are no visibly blurred features, local reconstruction of the simulation breaks down completely, and is less robust in the experimental case.

In Section 2 of Supplement 1 we perform an experiment with a sample composed of a variety of materials, which deviates strongly from the single-material assumption. While the global dark-field reconstruction has some difficulties in this case, the local reconstruction is still able to give a good qualitative picture of the strongly scattering components of the sample. In addition, based on the simulation carried out in Section 3, we saw that a local reconstruction can be more robust to noise than a global solution.

Interest in the spectral behavior of dark-field imaging has been spurred recently by progress in the development and proliferation of photon-counting energy-resolving X-ray detectors. A dichromatic or polychromatic source together with an energy-resolving detector would enable SPB-DF to be applied with a single exposure, significantly ameliorating issues with registration. A third energy bin raises the possibility of avoiding the single-material assumption, enabling separate reconstruction of the attenuation and refraction channels in multi-material samples. Multi-energy propagation-based imaging can be used to perform phase-retrieved material segmentation using a linearized transport-of-intensity equation [46]. This could be used to mitigate the attenuation artifacts that remain in our dark-field retrieval for multi-material samples, or could be extended to include dark-field effects based on our work. Imaging at additional energies may also allow for the extension of SPB-DF to directional dark-field imaging [65–68] by making an appropriate substitution of the scalar diffusion coefficient D, such as by a symmetric rank-2 diffusion tensor [55,69] of the form

$$D \rightarrow \begin{bmatrix} D_{xx} & \frac{1}{2} D_{xy} \\ \frac{1}{2} D_{xy} & D_{yy} \end{bmatrix}. \tag{18}$$

The imaging regime (energy, sample size) described within this paper is currently used in small-animal biomedical research studies [70], suggesting this approach could be of benefit in that work. Dual-energy X-ray imaging systems are already in widespread clinical and security use, raising the possibility that SPB-DF could be adopted for dark-field imaging in these contexts. To observe propagation-based dark-field effects, high local contrast would be helpful, which becomes more difficult at the higher energies and large pixel sizes used for human imaging. With a high-coherence micro-focus source and high-resolution detector, local image contrast can be achieved by imaging phase contrast speckle [71]. With a low-coherence source, one possibility is to overlay a high-contrast reference pattern, in the style of single-grid/speckle-based imaging, but without the explicit need for a mask-only reference image and the resulting strict set-up stability requirements. The resulting reconstruction would contain both the sample and the mask pattern, but this mask could then be subtracted out before image assessment. Commercial application would also require developing specific imaging protocols, including a choice of the dark-field energy dependence parameter. Further research is needed to assess if this is viable.

7. CONCLUSION

We have seen that dark-field effects are observable in propagation-based X-ray imaging, and that their strength changes with energy. We have developed a dual-energy imaging method of reconstructing the projected thickness of a sample that accounts for these dark-field effects using the X-ray Fokker–Planck model, improving the accuracy of reconstruction compared to TIE-based thickness reconstruction. Following the thickness reconstruction, we considered two methods of recovering the Fokker–Planck diffusion coefficient to give a dark-field image. A global method using Fourier transforms gives smooth qualitative solutions with low artifacts, but is susceptible to noise. An alternative method, comparing the visibility of local sample features in a raw image and a generated dark-field-free image, produces stronger artifacts, but gives quantitative results and is robust to both noise and multi-material samples. Further research is needed to develop robust methods for the general inverse problem of diffusion retrieval in dark-field imaging. Multi-energy reconstruction opens the door to using energy-discriminating detectors for single-exposure and time-resolved dark-field PBI.

Funding. National Health and Medical Research Council (IMPACT); Australian Research Council (DP230101327, FT18010037); Australian Nuclear Science and Technology Organisation (18515, 18648, 21352).

Acknowledgment. The work of Jannis Ahlers is supported by an Australian Government Research Training Program (RTP) Scholarship. We thank David Paganin and Henriette Bast for useful discussions, and Ying Ying How for sharing her single-grid dark-field retrieval code [60]. The experiments were completed at the Australian Synchrotron, part of ANSTO, under proposals 18515, 18648, and 21352. The authors are grateful for the help provided by Chris Hall, Daniel Hausermann, Anton Maksimenko, and Matthew Cameron, the beamline scientists at the Imaging and Medical Beamline.

Disclosures. The authors declare no conflicts of interest.

Data availability. Data underlying the results presented in this paper are not publicly available at this time but may be obtained from the authors upon reasonable request.

Supplemental document. See Supplement 1 for supporting content.

REFERENCES

1. R. Smith-Bindman, D. L. Miglioretti, E. Johnson, *et al.*, “Use of diagnostic imaging studies and associated radiation exposure for patients enrolled in large integrated health care systems, 1996-2010,” J. Am. Med. Assoc. **307**, 2400–2409 (2012).
2. D. Paganin, *Coherent X-Ray Optics*, Oxford Series on Synchrotron Radiation (Oxford University, 2006).
3. M. J. Kitchen, G. A. Buckley, T. E. Gureyev, *et al.*, “CT dose reduction factors in the thousands using X-ray phase contrast,” Sci. Rep. **7**, 15953 (2017).

4. Z. Zhong, W. Thomlinson, D. Chapman, *et al.*, "Implementation of diffraction-enhanced imaging experiments: At the NSLS and APS," Nucl. Instrum. Methods Phys. Res. A **450**, 556–567 (2000).
5. F. Pfeiffer, M. Bech, O. Bunk, *et al.*, "Hard-X-ray dark-field imaging using a grating interferometer," Nat. Mater. **7**, 134–137 (2008).
6. F. Yang, F. Prade, M. Griffa, *et al.*, "Dark-field X-ray imaging of unsaturated water transport in porous materials," Appl. Phys. Lett. **105**, 154105 (2014).
7. A. Yaroshenko, K. Hellbach, A. O. Yildirim, *et al.*, "Improved in vivo assessment of pulmonary fibrosis in mice using X-ray dark-field radiography," Sci. Rep. **5**, 17492 (2015).
8. M. J. Kitchen, G. A. Buckley, L. T. Kerr, *et al.*, "Emphysema quantified: mapping regional airway dimensions using 2D phase contrast X-ray imaging," Biomed. Opt. Express **11**, 4176–4190 (2020).
9. F. G. Meinel, F. Schwab, A. Yaroshenko, *et al.*, "Lung tumors on multimodal radiographs derived from grating-based X-ray imaging—a feasibility study," Phys. Med. **30**, 352–357 (2014).
10. Z. Wang, N. Hauser, G. Singer, *et al.*, "Non-invasive classification of microcalcifications with phase-contrast X-ray mammography," Nat. Commun. **5**, 3797 (2014).
11. E.-M. Braig, N. Roiser, M. A. Kimm, *et al.*, "X-ray dark-field radiography: potential for visualization of monosodium urate deposition," Investig. Radiol. **55**, 494–498 (2020).
12. E. Pagot, P. Cloetens, S. Fiedler, *et al.*, "A method to extract quantitative information in analyzer-based x-ray phase contrast imaging," Appl. Phys. Lett. **82**, 3421–3423 (2003).
13. L. Rigon, F. Arfelli, and R.-H. Menk, "Generalized diffraction enhanced imaging to retrieve absorption, refraction and scattering effects," J. Phys. D **40**, 3077–3089 (2007).
14. M. J. Kitchen, D. M. Paganin, K. Uesugi, *et al.*, "X-ray phase, absorption and scatter retrieval using two or more phase contrast images," Opt. Express **18**, 19994–20012 (2010).
15. C. David, B. Nöhammer, H. H. Solak, *et al.*, "Differential x-ray phase contrast imaging using a shearing interferometer," Appl. Phys. Lett. **81**, 3287–3289 (2002).
16. A. Momose, S. Kawamoto, I. Koyama, *et al.*, "Demonstration of X-ray Talbot interferometry," Jpn. J. Appl. Phys. **42**, L866–L868 (2003).
17. M. Endrizzi, P. C. Diemoz, T. P. Millard, *et al.*, "Hard X-ray dark-field imaging with incoherent sample illumination," Appl. Phys. Lett. **104**, 024106 (2014).
18. A. Olivo, "Edge-illumination x-ray phase-contrast imaging," J. Phys. Condens. Matter **33**, 363002 (2021).
19. H. H. Wen, E. E. Bennett, R. Kopace, *et al.*, "Single-shot x-ray differential phase contrast and diffraction imaging using two-dimensional transmission gratings," Opt. Lett. **35**, 1932–1934 (2010).
20. K. S. Morgan, D. M. Paganin, and K. K. W. Siu, "Quantitative single-exposure x-ray phase contrast imaging using a single attenuation grid," Opt. Express **19**, 19781–19789 (2011).
21. S. Bérujon, E. Ziegler, R. Cerbino, *et al.*, "Two-dimensional X-ray beam phase sensing," Phys. Rev. Lett. **108**, 158102 (2012).
22. K. S. Morgan, D. M. Paganin, and K. K. W. Siu, "X-ray phase imaging with a paper analyzer," Appl. Phys. Lett. **100**, 124102 (2012).
23. E. S. Dreier, A. Bergamaschi, G. K. Kallon, *et al.*, "Tracking based, high-resolution single-shot multimodal x-ray imaging in the laboratory enabled by the sub-pixel resolution capabilities of the MÖNCH detector," Appl. Phys. Lett. **117**, 264101 (2020).
24. S. Berujon, H. Wang, and K. Sawhney, "X-ray multimodal imaging using a random-phase object," Phys. Rev. A **86**, 063813 (2012).
25. M.-C. Zdora, P. Thibault, T. Zhou, *et al.*, "X-ray phase-contrast imaging and metrology through unified modulated pattern analysis," Phys. Rev. Lett. **118**, 203903 (2017).
26. D. M. Paganin, H. Labriet, E. Brun, *et al.*, "Single-image geometric-flow x-ray speckle tracking," Phys. Rev. A **98**, 053813 (2018).
27. K. M. Pavlov, H. T. Li, D. M. Paganin, *et al.*, "Single-shot X-ray speckle-based imaging of a single-material object," Phys. Rev. Appl. **13**, 054023 (2020).
28. M. R. Teague, "Deterministic phase retrieval: a Green's function solution," J. Opt. Soc. Am. **73**, 1434–1441 (1983).
29. D. M. Paganin and K. S. Morgan, "X-ray Fokker–Planck equation for paraxial imaging," Sci. Rep. **9**, 17537 (2019).
30. K. S. Morgan and D. M. Paganin, "Applying the Fokker–Planck equation to grating-based x-ray phase and dark-field imaging," Sci. Rep. **9**, 17465 (2019).
31. K. M. Pavlov, D. M. Paganin, H. T. Li, *et al.*, "X-ray multi-modal intrinsic-speckle-tracking," J. Opt. **22**, 125604 (2020).
32. S. J. Alloo, D. M. Paganin, K. S. Morgan, *et al.*, "Dark-field tomography of an attenuating object using intrinsic x-ray speckle tracking," J. Med. Imaging **9**, 031502 (2022).
33. A. Snigirev, I. Snigireva, V. Kohn, *et al.*, "On the possibilities of x-ray phase contrast microimaging by coherent high-energy synchrotron radiation," Rev. Sci. Instrum. **66**, 5486–5492 (1995).
34. P. Cloetens, R. Barrett, J. Baruchel, *et al.*, "Phase objects in synchrotron radiation hard x-ray imaging," J. Phys. D **29**, 133–146 (1996).
35. S. W. Wilkins, T. E. Gureyev, D. Gao, *et al.*, "Phase-contrast imaging using polychromatic hard X-rays," Nature **384**, 335–338 (1996).
36. D. Paganin, S. C. Mayo, T. E. Gureyev, *et al.*, "Simultaneous phase and amplitude extraction from a single defocused image of a homogeneous object," J. Microsc. **206**, 33–40 (2002).
37. D. M. Paganin, V. Favre-Nicolin, A. Mirone, *et al.*, "Boosting spatial resolution by incorporating periodic boundary conditions into single-distance hard-x-ray phase retrieval," J. Opt. **22**, 115607 (2020).
38. T. E. Gureyev, D. M. Paganin, B. Arhatari, *et al.*, "Dark-field signal extraction in propagation-based phase-contrast imaging," Phys. Med. Biol. **65**, 215029 (2020).
39. A. Aminzadeh, B. D. Arhatari, A. Maksimenko, *et al.*, "Imaging breast microcalcifications using dark-field signal in propagation-based phase-contrast tomography," IEEE Trans. Med. Imaging **41**, 2980–2990 (2022).
40. T. A. Leatham, D. M. Paganin, and K. S. Morgan, "X-ray dark-field and phase retrieval without optics, via the Fokker–Planck equation," IEEE Trans. Med. Imaging **42**, 1681–1695 (2023).
41. R. D. Speller, G. J. Ensell, and C. Wallis, "A system for dual-energy radiography," Br. J. Radiol. **56**, 461–465 (1983).
42. H. Alkadhi, A. Euler, D. Maintz, *et al.*, eds., *Spectral Imaging: Dual-Energy, Multi-Energy and Photon-Counting CT, Medical Radiology* (Springer, 2022).
43. R. E. Alvarez and A. Macovski, "Energy-selective reconstructions in X-ray computerised tomography," Phys. Med. Biol. **21**, 733–744 (1976).
44. T. E. Gureyev and S. W. Wilkins, "On X-ray phase retrieval from polychromatic images," Opt. Commun. **147**, 229–232 (1998).
45. T. E. Gureyev, S. Mayo, S. W. Wilkins, *et al.*, "Quantitative in-line phase-contrast imaging with multienergy X rays," Phys. Rev. Lett. **86**, 5827–5830 (2001).
46. F. Schaff, K. S. Morgan, J. A. Pollock, *et al.*, "Material decomposition using spectral propagation-based phase-contrast X-ray imaging," IEEE Trans. Med. Imaging **39**, 3891–3899 (2020).
47. F. Schaff, J. A. Pollock, K. S. Morgan, *et al.*, "Spectral propagation-based x-ray phase-contrast computed tomography," J. Med. Imaging **9**, 031506 (2022).
48. K. Taphorn, F. De Marco, J. Andrejewski, *et al.*, "Grating-based spectral X-ray dark-field imaging for correlation with structural size measures," Sci. Rep. **10**, 13195 (2020).
49. T. Partridge, A. Astolfo, S. S. Shankar, *et al.*, "Enhanced detection of threat materials by dark-field x-ray imaging combined with deep neural networks," Nat. Commun. **13**, 4651 (2022).
50. K. Taphorn, L. Kaster, T. Sellerer, *et al.*, "Spectral X-ray dark-field signal characterization from dual-energy projection phase-stepping data with a Talbot-Lau interferometer," Sci. Rep. **13**, 767 (2023).
51. T. Sellerer, K. Mechlem, R. Tang, *et al.*, "Dual-energy X-ray dark-field material decomposition," IEEE Trans. Med. Imaging **40**, 974–985 (2021).
52. G. Pelzer, A. Zang, G. Anton, *et al.*, "Energy weighted x-ray dark-field imaging," Opt. Express **22**, 24507–24515 (2014).
53. A. A. Michelson, *Studies in Optics*, University of Chicago Science Series (The University of Chicago, 1927).
54. M.-C. Zdora, "State of the art of X-ray speckle-based phase-contrast and dark-field imaging," J. Imaging **4**, 60 (2018).
55. D. M. Paganin, D. Pelliccia, and K. S. Morgan, "Paraxial diffusion-field retrieval," Phys. Rev. A **108**, 013517 (2023).
56. K. S. Morgan, K. K. W. Siu, and D. M. Paganin, "The projection approximation and edge contrast for x-ray propagation-based phase contrast imaging of a cylindrical edge," Opt. Express **18**, 9865–9878 (2010).
57. L. Quénot, H. Rougé-Labriet, S. Bohic, *et al.*, "Implicit tracking approach for X-ray phase-contrast imaging with a random mask and a conventional system," Optica **8**, 1412–1415 (2021).
58. H. Labriet, S. Berujon, and E. Brun, "X-ray imaging device and associated imaging method," Patent WO/2021/005283 (14 January 2021).

59. T. Schoonjans, A. Brunetti, B. Golosio, *et al.*, “The xraylib library for X-ray—matter interactions. Recent developments,” Spectrochim. Acta B **66**, 776–784 (2011).
60. Y. Y. How and K. S. Morgan, “Quantifying the x-ray dark-field signal in single-grid imaging,” Opt. Express **30**, 10899–10918 (2022).
61. A. W. Stevenson, J. C. Crosbie, C. J. Hall, *et al.*, “Quantitative characterization of the X-ray beam at the Australian Synchrotron Imaging and Medical Beamline (IMBL),” J. Synchrotron Radiat. **24**, 110–141 (2017).
62. G. D. Evangelidis and E. Z. Psarakis, “Parametric image alignment using enhanced correlation coefficient maximization,” IEEE Trans. Pattern Anal. Mach. Intell. **30**, 1858–1865 (2008).
63. K. Taphorn, K. Mechlem, T. Sellerer, *et al.*, “Direct differentiation of pathological changes in the human lung parenchyma with grating-based spectral X-ray dark-field radiography,” IEEE Trans. Med. Imaging **40**, 1568–1578 (2021).
64. T. A. Leatham, D. M. Paganin, and K. S. Morgan, “X-ray phase and dark-field computed tomography without optical elements,” Opt. Express **32**, 4588–4602 (2024).
65. T. H. Jensen, M. Bech, O. Bunk, *et al.*, “Directional x-ray dark-field imaging,” Phys. Med. Biol. **55**, 3317–3323 (2010).
66. M. Kagias, Z. Wang, P. Villanueva-Perez, *et al.*, “2D-omnidirectional hard-X-ray scattering sensitivity in a single shot,” Phys. Rev. Lett. **116**, 093902 (2016).
67. R. Smith, F. D. Marco, L. Broche, *et al.*, “X-ray directional dark-field imaging using unified modulated pattern analysis,” PLOS ONE **17**, e0273315 (2022).
68. M. K. Croughan, Y. Y. How, A. Pennings, *et al.*, “Directional dark-field retrieval with single-grid x-ray imaging,” Opt. Express **31**, 11578–11597 (2023).
69. K. M. Pavlov, D. M. Paganin, K. S. Morgan, *et al.*, “Directional dark-field implicit x-ray speckle tracking using an anisotropic-diffusion Fokker-Planck equation,” Phys. Rev. A **104**, 053505 (2021).
70. K. S. Morgan, D. Parsons, P. Cmielewski, *et al.*, “Methods for dynamic synchrotron X-ray respiratory imaging in live animals,” J. Synchrotron Radiat. **27**, 164–175 (2020).
71. M. J. Kitchen, D. Paganin, R. A. Lewis, *et al.*, “On the origin of speckle in x-ray phase contrast images of lung tissue,” Phys. Med. Biol. **49**, 4335–4348 (2004).